Regular dendritic patterns induced by nonlocal time-periodic forcing

T. Börzsönyi,[1,2] T. Tóth-Katona,[1] Á. Buka,[1] and L. Gránásy[1]

[1]*Research Institute for Solid State Physics and Optics, Hungarian Academy of Sciences, P.O.B. 49, H-1525 Budapest, Hungary*

[2]*Groupe de Physique des Solides, CNRS UMR No. 75-88, Universités Paris VI et VII, Tour 23, 2 place Jussieu, 75251 Paris Cedex 05, France*

The dynamic response of dendritic solidification to spatially homogeneous time-periodic forcing has been studied. Phase-field calculations performed in two dimensions (2D) and experiments on thin (quasi-2D) liquid-crystal layers show that the frequency of dendritic side branching can be tuned by oscillatory pressure or heating. The sensitivity of this phenomenon to the relevant parameters, the frequency and amplitude of the modulation, the initial undercooling and the anisotropies of the interfacial free energy, and molecule attachment kinetics, has been explored. It has been demonstrated that in addition the side-branching mode synchronous with external forcing as emerging from the linear Wentzel-Kramers-Brillouin analysis, modes that oscillate with higher harmonic frequencies are also present with perceptible amplitudes.

PACS number(s): 05.45.Xt, 81.10.Aj, 64.70.Dv, 68.70.+w

I. INTRODUCTION

Complex patterns observed in nature have attracted considerable interest recently [1–3]. The complicated spatiotemporal behavior that leads to the formation of such patterns is usually associated with the instabilities of systems transforming under nonequilibrium conditions. A spectacular example of practical importance is dendritic growth that appears in anisotropic systems where the propagation of the transformation front is coupled with the diffusion of a conserved quantity. The respective diffusional instabilities lead to the formation of a traveling quasisteady-state tip that emits surface undulations which evolve into side arms in directions determined by the anisotropy of the system [4]. Many of the technologically important materials form by dendritic solidification [4]. Analogous phenomena have been reported in biological systems [5], anisotropic Hele-Shaw cells [6], and in cosmology-particle physics [7,8]. Although experiments on the freezing of transparent liquids [9–14] clarified many of the essential features of dendrite formation, important questions remained open. For example, the role played by thermal fluctuations in side branching is the subject of continuing investigations [4,13,15–18]. It is anticipated that a selective amplification of thermal noise is responsible for the side branching and for the observed irregularity of dendritic patterns [10–12,19].

While the steady-state behavior of dendritic growth is understood fairly well in the framework of recent theories (microscopic solvability [4,20–22] and phase-field theories [4,23–28]), less is known of the dynamic response of the dendritic morphology to time-dependent external perturbations. The nonlinear systems often develop regular patterns under periodic forcing [3]. Considering the inherent nonlinearity of the equations describing dendritic growth, it is reasonable to expect that such periodic perturbations lead to resonance patterns that might be used to influence the growth morphology. Besides its scientific interest, a detailed understanding of such phenomena could open novel routes for designing materials for specific applications.

Time-periodic forcing of dendritic side branching has already been realized via local heating of the dendrite tip by laser beam [29–31] (which has the advantage of being well controllable but cannot be applied homogeneously in large volumes), or by exposing it to an oscillatory flow field [32] (which is global, but spatially homogeneous forcing cannot be easily achieved). Both methods lead to the formation of fairly regular morphologies in a suitable frequency range. However, these methods cannot be easily used for spatially homogeneous controlling of growth morphologies in large volumes. To circumvent this problem, we demonstrated [33] the possibility for tuning the dendritic morphology by spatially homogeneous time periodic forcing via modulated pressure [34,35] and heating, that change the undercooling instantaneously and homogeneously in large volumes.

In this paper we present a detailed analysis of the dynamic response of dendritic solidification to oscillating pressure and heating. In identifying the resonance conditions and the most important process parameters, we rely on phase-field modeling, one of the most potent methods for describing morphology evolution. The theoretical predictions will be confronted with experiments on quasi-two-dimensional (2D) liquid crystal layers, known as suitable model materials [14,36–38]. The rest of this paper is structured as follows. In Sec. II we briefly summarize the phase-field equations that incorporate external forcing, and introduce quantities for characterizing growth morphology. Section III is devoted to the experimental setup and the details of the measurement techniques. In Sec. IV, we present the phase-field predictions and compare them with the experimental results. In Sec. V, our findings are discussed in the light of theory and experiment on tip-localized forcing. Finally, a few concluding remarks will be made in Sec. VI.

II. PHASE-FIELD THEORY WITH EXTERNAL FORCING

We investigate the growth of the crystalline phase into an undercooled single component liquid at a temperature between the melting point and the hypercooling limit (''unit undercooling'') [39]. In this temperature range, the thermal diffusion controls the growth process, as opposed to the (molecule attachment) kinetics controlled mechanism taking

place below the hypercooling temperature [40]. Owing to the heat release during solidification, the crystalline phase heats up to its melting point, while the rest of the latent heat is transported into the cold liquid. Under such conditions, the planar front is inherently unstable against thermal perturbations despite the stabilizing effect of the interfacial free energy [41].

The phase-field theory is a powerful tool with which to study moving boundary problems. It represents a dynamic extension of the Cahn-Hilliard theory of first-order phase transformations, in which the evolution of a nonconserved order parameter is coupled to thermal or chemical diffusion [4,23–28]. Here we use a thermodynamically consistent version [23] (model I of Ref. [25]) which ensures locally positive entropy production and was modified to incorporate anisotropies of the interfacial free energy and the kinetic coefficient [42]. The local state of the matter is represented by the phase field $\phi(\mathbf{r},t)$ [43].

To incorporate external forcing, the equations [25,42] that describe the evolution of the phase field and the temperature field $T(\mathbf{r},t)$ in 2D

$$\tau(\theta)\frac{\partial\phi}{\partial t} = Q(T)p'(\phi) - G'(\phi) - \frac{\delta}{\delta\phi}\left\{\frac{1}{2}[\kappa(\theta)]^2|\nabla\phi|^2\right\},$$

(2.1)

$$\{c_p + [p(\phi)-1]L'(T)\}\frac{\partial T}{\partial t} + L(T)p'(\phi)\frac{\partial\phi}{\partial t} = k\nabla^2 T,$$

(2.2)

have to be modified. Here τ is an empirical relaxation coefficient, whose inverse is an intrinsic interfacial mobility, and $\delta/\delta\phi$ stands for variation with respect to ϕ. Other notations are as follows: $p(\phi) = \phi^3(10 - 15\phi + 6\phi^2)$, $\kappa^2/2$ the coefficient of the square-gradient term in the entropy functional, that depends on the orientation represented by the angle θ (defined as $\tan(\theta) = \partial_y\phi/\partial_x\phi$), $G(\phi) = \phi^2(1-\phi)^2/4e$, e is a constant that determines the height of the intermediate maximum of the double well potential $Q(T) = \int_{T_m}^T [L(\eta)/\eta^2]d\eta = -\Delta G(T)/T$, $\Delta G(T)$ the Gibbs free energy difference between the liquid and solid, while c_p, $L(T)$, and k are the specific heat of the liquid, the enthalpy difference between the liquid and the solid, and the thermal conductivity, respectively. The primed quantities denote derivatives with respect to the arguments. Note that ϕ and p are dimensionless. The units of k and κ^2 are W m^{-1} K^{-1} and J m^{-1} K^{-1}, respectively; while Q, G, c_p, and $1/e$ are measured in J m^{-3} K^{-1}.

The dominant effect of the pressure modulation $p(t) = p_0 + \Delta p(t)$ is a variation of the melting point described by the Clausius-Clapeyron law $T_m(p) = T_m(p_0) + \Delta p\Delta V/S_m$, where ΔV is the volume change upon solidification and S_m is the entropy of fusion. This enters into Eq. (1) via the Gibbs free energy difference which may be approximated as $\Delta G(T,p) \approx S_m[T_m(p)-T]$ at small undercoolings ($T_m - T \ll T_m$). The other relevant quantities [specific heat, heat of fusion, and entropy of fusion $L'(T)$] are far less sensitive to the variation of pressure. For example, integrating the Clausius-Clapeyron relationship one obtains $\Delta L = \Delta p\Delta V[1 + \Delta c_p/S_m + T(\alpha_l V_l - \alpha_s V_s)/\Delta V]$, where $\Delta c_p = c_{p,l} - c_{p,s}$ is

the variation of the specific heat upon melting, $\alpha_{l,s}$ are the thermal expansion coefficients, while subscripts l and s refer to the liquid and the solid respectively. Under typical conditions of our experiments [pressure amplitude ~ 2 bar, undercooling of 1 K, and physical properties of CCH3 (Appendix)], the undercooling varies by $\sim 6\%$, while the relative change of L (and S_m) is only $\sim 10^{-3}$. We found that such pressure effects on L and S_m do not influence the results perceptibly; i.e., pressure modulation needs to be taken into account only via $Q(T)$ in Eq. (1). Modulated heating, in turn, appears as a time dependent source term in Eq. (2).

At this stage it is advantageous to introduce dimensionless variables. This is done by using a characteristic length scale ω (comparable to the size of a well developed crystallite) and the thermal diffusion time ω^2/D where D is the thermal diffusion coefficient. To avoid complications emerging from an oscillating melting point, the reduced temperature has been redefined in terms of a constant reference temperature T_r as $u(\mathbf{r},t) = (T-T_r)/(T_r - T_\infty)$, where T_∞ is the initial temperature of the undercooled liquid. The mathematical problem is invariant to the choice of T_r so far as $A = u_m = (T_m - T_r)/(T_r - T_\infty)$ is inserted as in Eq. (3). (With $T_r = T_m$, the usual form of the phase-field model is recovered.)

The relevant physical properties are combined into dimensionless parameters $\Delta = c_p(T_r - T_\infty)/L$, $\alpha = \sqrt{2}\omega S_m L/(12c_p\sigma_0)$, $\tau_0 = S_m D\beta_0/\sigma_0$, and $\epsilon = \delta/\omega$, $\tilde{\sigma}' = d\tilde{\sigma}/d\theta$, where δ is the interface thickness. The anisotropies of the interfacial free energy σ and the kinetic coefficient β are represented by the dimensionless functions $\tilde{\sigma} = 1 + \sigma_n\cos(n\theta)/2$ and $\tilde{\beta} = 1 + \beta_n\cos(n\theta)/2$ of n-fold symmetry, that are related to the dimensional quantities via relationships $\sigma(\theta) = \sigma_0\tilde{\sigma}(\theta)$ and $\beta(\theta) = \beta_0\tilde{\beta}(\theta)$. Here σ_n and β_n are the anisotropy parameters. Lengths and time are scaled by ω and ω^2/D, respectively. The coefficient κ and the constant e are related to δ and the interfacial free energy [25].

With these notations Eqs. (1) and (2) transform to

$$\epsilon^2\tau_0\tilde{\beta}\tilde{\sigma}\frac{\partial\phi}{\partial t} = \phi(1-\phi)\left\{\phi - \frac{1}{2} + 30\epsilon\alpha\Delta[u-A(t)]\phi\right.$$

$$\left.\times(1-\phi)\right\} - \epsilon^2\frac{\partial}{\partial x}\left[\tilde{\sigma}\tilde{\sigma}'\frac{\partial\phi}{\partial y}\right] + \epsilon^2\frac{\partial}{\partial y}$$

$$\times\left[\tilde{\sigma}\tilde{\sigma}'\frac{\partial\phi}{\partial x}\right] + \epsilon^2\nabla[\tilde{\sigma}^2\nabla\phi],$$

(2.3)

$$\frac{\partial u}{\partial t} + \frac{1}{\Delta}30\phi^2(1-\phi)^2\frac{\partial\phi}{\partial t} = \nabla^2 u + B(t),$$

(2.4)

where the modulated pressure and heating are incorporated via terms $A(t)$ and $B(t)$, respectively.

In this work Eqs. (2.3),(2.4) have been solved numerically on an $N\times N$ rectangular grid, $N = 1000$, that corresponds to an area $l\times l$ of dimensionless linear size $l = 5$ and a grid spacing $\Delta x = 0.005$. An explicit finite difference scheme has been employed in the case of Eq. (2.3), while Eq. (2.4) has been handled by the alternating-direction implicit method which is unconditionally stable [42]. At $t = 0$ a crystalline nucleus ($\phi = 0$) is placed at the center of the model area filled by uniformly undercooled liquid ($\phi = 1$, $u = -1$). The

reduced temperature and the phase field were kept constant ($u = -1$ and $\phi = 1$) at the boundaries of the model space. To save CPU time, we used a primitive adaptive mesh technique: far from the solidification front Eq. (2.4) has been solved on a rough grid (of spacing $10 \times \Delta x$). To model the effect of thermal fluctuations and to suppress undesirable lattice effects that favor specific growth directions, a spatially and temporally uncorrelated noise of amplitude 0.01 and zero mean value has been added to the dimensionless temperature u in every time step. If not stated otherwise, we use the dimensionless parameters: $\alpha = 350$, $\tau_0 = 20$, $\epsilon = 0.005$, $\Delta x = 0.005$, and time step $\Delta t = 10^{-4}$. Owing to the known limitations of phase-field modeling [4,44], we performed our calculations at relatively large undercoolings, $\Delta = 0.40 - 0.68$.

To characterize the spatiotemporal behavior of the evolving dendritic morphology the following quantities were determined.

(1) We measured the width w of the dendrite behind the tip at a distance of $\zeta = 0.75$ (150 pixels). To investigate this feature for longer times, we performed separate simulations on a 1200×600 grid, oriented so that the larger dimension be parallel with the direction of growth (here we used $\Delta t = 8 \times 10^{-5}$). The amplitude A_ν in the Fourier transform $W(f)$ of $w(t)$ characterizes the response synchronous with external forcing.

(2) The symmetry of the growth patterns was characterized by the quantities a and b:

$$a = \frac{\Sigma_{i,j=-N/2}^{N/2}(\phi_{i,j} - \phi_{-i,j})^2}{M},\qquad(2.5)$$

$$b = \frac{\Sigma_{i,j=-N/2}^{0}(\phi_{i,j} - \phi_{j,i})^2}{K},\qquad(2.6)$$

where M and K are the numbers of pixels in which $0.4 < \phi < 0.6$ for the whole system and for the lower left quarter, respectively. Accordingly, $a \geq 0$ measures the symmetry of the whole domain with respect to the y axis, while $b \geq 0$ quantifies the axisymmetry of a main branch. Both parameters are zero for symmetric patterns.

III. EXPERIMENTAL SETUP AND CONDITIONS

The nematic–smectic-B ($N - S_B$) phase transition of liquid crystals is recognized as an appropriate model of crystallization in liquids [36–38]. A specialty of this phase transformation is a large anisotropy of the interfacial free energy [37], a property expected to be advantageous for the regularization of dendritic morphology on theoretical grounds (see Sec. IV A and Ref. [33]).

To test the predictions, experiments have been performed on thin CCH3 liquid crystal layers. Ready-made cells of E.H.C. Co. (Japan) KSRP-10 (of thickness 10 μm) and KSRP-02 (2 μm) have been filled with CCH3 (Merck, Darmstadt). To investigate whether modulated pressure induces flow in the experiments, we tracked the position/motion of tracer particles. With the exception when bubbles were trapped in the liquid crystal, we were unable to detect fluid flow in our 2 μm cells. All experiments were performed
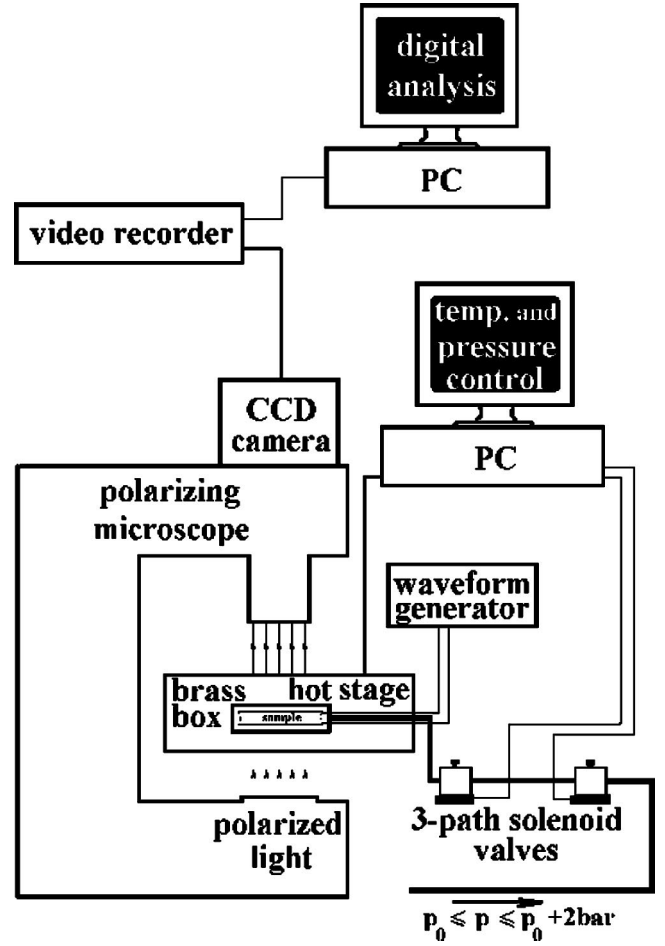

FIG. 1. Experimental setup.

on bubble free cells. The surface treatment of the bounding glass plates assured the planar alignment of both N and S_B phases [the directors $\mathbf{n}(N)$ and $\mathbf{n}(S_B)$ that describe the average orientation of the elongated molecules are in the plane of the cell], and the conducting layers on the bounding plates were used as electrodes.

For pressure modulation the liquid crystal cell was placed into a brass box (see Fig. 1) surrounded by a temperature controlled hot stage of accuracy ± 3 mK. The gas pressure in the brass box has been regulated by a computer controlled solenoid valve system that switches on and off an excess pressure p_e preset between 0 to 2 bar with an accuracy of ± 0.03 bar. This allows square wavelike pressure modulations in the frequency range up to $\tilde{\nu} \sim 2$ Hz.

The modulated heat release in the bulk has been realized by periodically transmitting a high frequency (600 kHz) electric current through the liquid crystal layer produced by gating the signal of a function generator with $\tilde{\nu} \sim 1$ Hz. The local off-plane heat transport (a precondition of regulation with oscillatory heating, see Sec. IV A and Ref. [33]) is ensured by the quasi-2D sample geometry and by the heat transport through the bounding glass plates.

The growth patterns were monitored in transmitting mode via a polarizing microscope equipped with a CCD camera, a method relying on the different optical properties of the nematic and smectic B phases. The images were stored and processed by a PC. The spatial and time resolutions of the
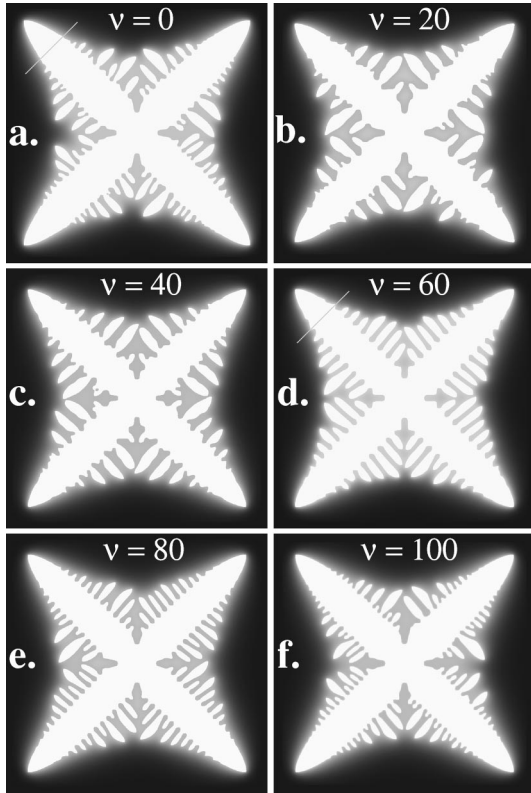
FIG. 2. Dendritic patterns of fourfold symmetry predicted by the phase-field theory for $\Delta=0.6$, $\sigma_4=-0.12$, $\beta_4=0.24$, and $t=0.22$. (a) Under constant pressure yielding $A=u_m=0.048$ and (b)–(f) in the presence of square-wave pressure modulations of amplitude $a_0=0.16$ and filling coefficient $\xi=0.3$. The gray level in the liquid phase indicates the temperature field. The white line marks the position, where the width of the dendrite arm was measured. System size: 1000×1000 pixels.

system were 512×512 pixels and 0.04 s, respectively. The calibration procedure with $6.3\times$ objective and $3.2\times$ projector combination gave scale factors of 1.35 ± 0.01 μm/pixel in the x direction and 0.95 ± 0.01 μm/pixel in the y direction.

The same setup has been used to measure the pressure coefficient of the temperature of transformation between the smectic-B and nematic phases (see the Appendix).

IV. RESULTS

A. Theoretical predictions

To find resonance patterns we investigated the parameter space defined by the frequency and amplitude of the modulation, the undercooling and the anisotropies of the interfacial free energy and the kinetic coefficient. The calculations were performed with fourfold and sixfold anisotropies ($n=4$ and 6 in expressions for $\tilde{\sigma}$ and $\tilde{\beta}$). Before presenting our results on nonlocal periodic forcing we characterize the unmodulated *reference* state.

1. Free dendritic growth

Independently of the symmetry of the system, a weak uncorrelated (noise-induced) side-branching occurs in the unmodulated reference state shown in Fig. 2(a). The width $w(t)$ of a main dendrite arm measured at a dimensionless
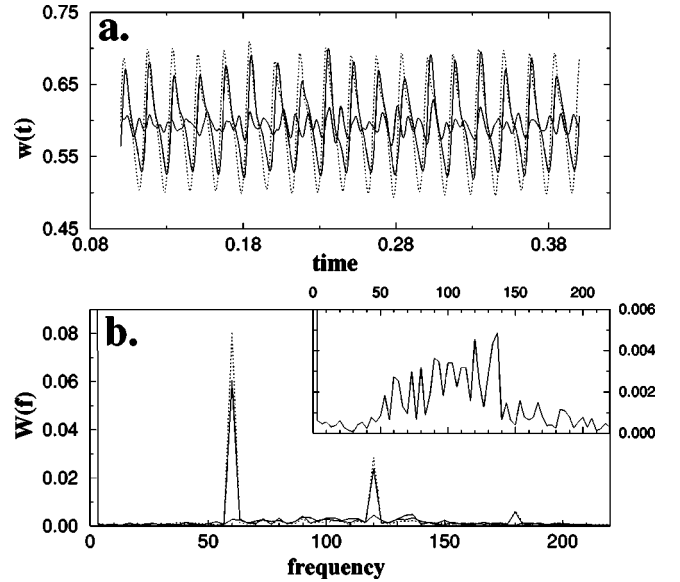

FIG. 3. (a) Width of the dendrite $w(t)$ at a distance of $\zeta=0.75$ behind the dendrite tip without periodic perturbation [heavy solid line; Fig. 2(a)], in the presence of sinusoidal (light solid line) and square-wave [dotted line; Fig. 2(d)]. (b) The respective Fourier spectra $W(f)$.

distance of $\zeta=0.75$ behind the tip [Fig. 3(a)] indicates surface undulations that can be decomposed into a spectrum of oscillations which covers the dimensionless frequency range of ~30 to ~170, centered around a characteristic frequency of $f_0\sim100$ [see inset in Fig. 3(b)]. This behavior accords with that seen in the phase-field simulations of Karma and Rappel [18], and with experimental results [16,30]. In agreement with Ref. [18], we find that far from the tip the characteristic wave length $\lambda_0=v/f_0$ depends much more weakly on the distance from the tip than predicted by the microscopic solvability theory [22,45], a behavior interpreted in terms of the "stretching" of the perturbations [18] that travel along the curved perimeter of the dendrite.

Considering that the applied uncorrelated noise probes the dynamic response of the system to a broad variety of frequencies, it is reasonable to seek "resonance" in the vicinity of the characteristic frequency f_0 of spontaneous side branching.

2. Pressure modulations

According to the Clausius-Clapeyron law, the modulated pressure translates into a time dependent melting point, and is represented by inserting $A(t)=u_m(t)=a_0g(t)$ and $B(t)=0$ into Eqs. (3) and (4). Since our experimental setup allows only square-wave modulations (characterized by the filling coefficient $\xi=t_{on}/t_0$, where t_0 is the period of oscillations and t_{on} the pulse length), the simulations have been performed for this wave form (unless stated otherwise).

(a) *The effect of forcing frequency.* The frequency dependence of the growth patterns is shown in Figs. 2(b)–2(f). At low forcing frequencies ($\nu<15$), the system alternates between two steady-state growth modes yielding uncorrelated side branching that correspond to the actual undercooling. It is, however, remarkable that the switching transient between the constant pressure stages initiates more pronounced side arms than formed during the constant pressure periods.
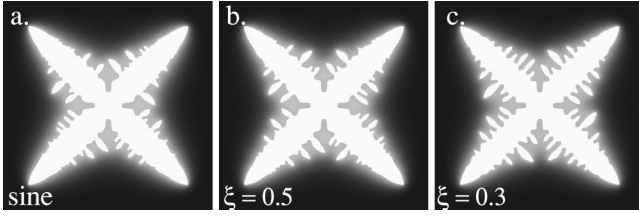
FIG. 4. Comparison of growth patterns corresponding to (a) sinusoidal, (b) symmetric ($\xi=0.5$), and (c) asymmetric ($\xi=0.3$) square-wave forcing of equal period lengths ($\nu=30$), and period averaged amplitudes for $\Delta=0.55$. Note the side-branch ''doubling'' in panel (c). (Other relevant parameters are as for Fig. 2.) System size: 1000×1000 pixels.

Regular growth morphologies [Fig. 2(b)–(e)] are observed in the lower half of the dimensionless frequency range of spontaneous thermal side branching shown in the inset of Fig. 3(b). At frequencies larger than these, the formation of side branches cannot follow the external forcing, and the uncorrelated thermal side branching reappears [Fig. 2(f)].

In agreement with our earlier results [33], when regular morphologies are formed, the side branching and the tip velocity correlate with the pressure modulation. The parameters $w(t)$, a, and b reflect the formation of regular morphologies. For example, a periodic variation of the width $w(t)$ of the dendrite is seen [Fig. 3(a)], which correlates with the external sinusoidal forcing and leads to the formation of regular side branches. Note that in addition to the forcing frequency [that appears with a far larger amplitude in $W(f)$ than the spontaneous undulations], its second and third harmonics ($2\nu,3\nu$) are also present albeit with an amplitude that diminishes for higher order harmonics [Fig. 3(b)].

Apparently, periodic forcing with fixed frequency excites several surface modulations; one synchronous with the forcing frequency (ν) and others oscillating with the higher harmonic frequencies ($2\nu,3\nu,\dots$), which indicates a dynamic coupling among these modes associated with the nonlinearity of the governing equations.

The relative amplitudes of higher harmonics vary with the wave form of the pressure modulation yielding different growth patterns (see Fig. 4). Fairly similar patterns [see Figs. 4 (a) and 4(b)] are observed for sinusoidal and square-wave modulations, provided that for the latter $\xi=0.5$ [i.e., frequencies $(2n+1)\nu$, $n=1,2,\dots$, are present in the forcing spectrum]. When the filling coefficient ξ deviates from 0.5, the frequency/phase content of forcing varies (e.g., the second harmonic 2ν appears) leading to such effects as the formation of side branches of twice the number corresponding to the base frequency [see Figs. 4(a)–4(c)]. To understand this behavior we analyze the frequency dependence of the dynamic response of the system to ''asymmetric'' forcing ($\xi=0.3$).

The Fourier amplitudes A_ν and $A_{2\nu}$ (corresponding to modes that oscillate with the forcing frequency and its double, respectively) and the symmetry parameters a and b are presented in Fig. 5 as a function of the forcing frequency ν. A_ν and $A_{2\nu}$ show maxima when ν or 2ν is close to $f_{exc}\sim70$ [Fig. 5(a)], where f_{exc} is the frequency where the synchronous response has the maximum amplitude. Note that f_{exc} is somewhat below the characteristic frequency $f_0\sim100$ of the unperturbed dendritic growth. A possible expla-
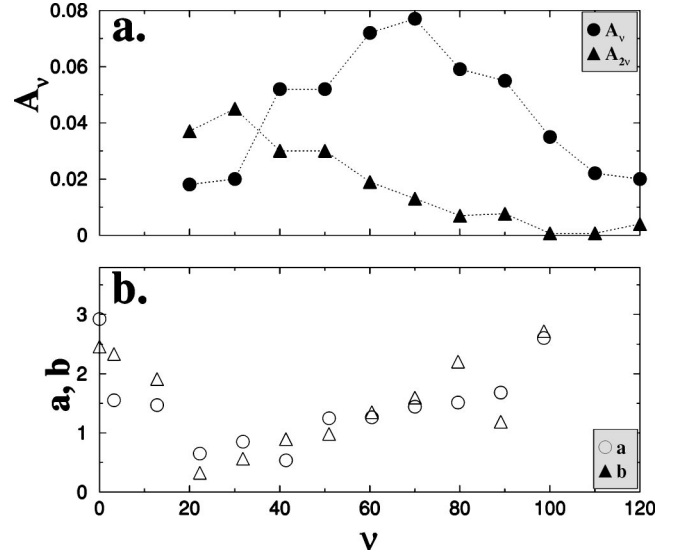

FIG. 5. Amplitude of Fourier peaks A_ν and $A_{2\nu}$ measured at $\zeta=0.75$ behind the tip, and the symmetry parameters a and b as a function of the driving frequency ν. Other relevant parameters are $\Delta=0.55$, $\xi=0.3$, $\sigma_4=-0.12$, and $\beta_4=0.24$, while $a_0=0.14$ (a) and $a_0=0.2$ (b).

nation of this deviation might be a different ''stretching'' of perturbations, related to differences seen between shapes of dendrite tips formed in free growth and under external forcing. It is also remarkable, that at low forcing frequencies the amplitude $A_{2\nu}$ of the second harmonic becomes larger than A_ν. This inversion of the relative magnitudes of A_ν and $A_{2\nu}$ is responsible for the side-branch ''doubling'' shown in Fig. 4. A similar phenomenon is seen in Fig. 2(b), where the second harmonic is the dominant mode as indicated by the striking similarity of patterns corresponding to $\nu=20$ and 40 [see Figs. 2(b) and 2(c)].

We find that the amplitude A_ν increases approximately exponentially with the distance ζ from the tip of the dendrite, while $A_{2\nu}$ saturates as a function of ζ (Fig. 6). Remarkably, the symmetry parameters a and b display minima at lower forcing frequencies [around $\nu\sim20$; see Fig. 5(b)] than the maximum of the Fourier amplitude A_ν. This difference in the positions of the extrema is a manifestation of the fact that axial symmetry and frequency content are different constituents of regularity. It appears that A_ν gives a closer representation of the regularity recognized by the human eye than the symmetry parameters. The overall frequency dependence of
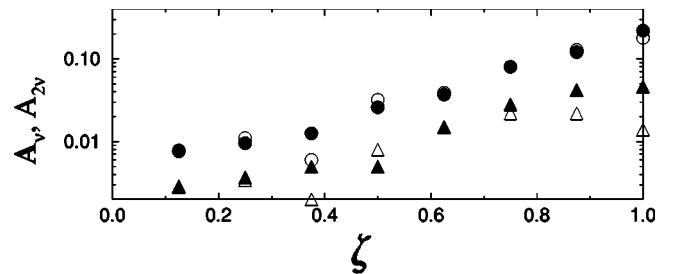

FIG. 6. Fourier amplitudes A_ν (circles) and $A_{2\nu}$ (triangles) as a function of the distance ζ from the dendrite tip at two undercoolings $\Delta=0.55$ (full symbols) and 0.6 (empty symbols). Note the roughly exponential behavior of A_ν and the saturation in $A_{2\nu}$. Other relevant parameters are $\nu=60$, $\xi=0.3$, $a_0=0.16$, $\sigma_4=-0.12$, and $\beta_4=0.24$.
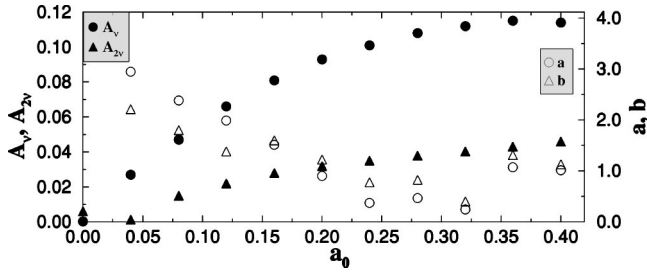
FIG. 7. Amplitude of the Fourier peaks A_ν and $A_{2\nu}$, and the symmetry parameters a and b as a function of the forcing amplitude a_0 for the system shown in Fig. 2(d).

the pattern formation supports our anticipation that regularization via periodic forcing with fixed frequencies is possible when the latter fall in the characteristic frequency range of noise-induced side branching.

(b) *The effect of the amplitude of forcing.* The Fourier amplitudes A_ν and $A_{2\nu}$ and the symmetry parameters show that with increasing forcing amplitude a_0 the regularity of the growth patterns increases (Fig. 7). This is manifested in monotonously increasing A_ν and $A_{2\nu}$ that saturate for large a_0. At the same time, a and b decrease with a_0, reflecting the increasing symmetry of the patterns.

(c) *The effect of undercooling.* The response to a given pressure modulation correlates with the tendency for ''natural'' side branching (Fig. 8). While at large undercoolings (e.g., $\Delta=0.65$), the formation of side branches is rather intense, leading to well developed side-arms (both with or without forcing), at $\Delta=0.5$ or below free growth produces essentially no side branches, and external forcing is needed to trigger them, also reflected in their smaller size. Note the difference in spatial periodicity, that originates from the temperature dependence of the tip velocity.

The variation of the Fourier amplitudes A_ν and $A_{2\nu}$ with undercooling (Δ) is shown in Fig. 9. The maximum of A_ν might be understood as follows. We found that with increasing undercooling f_{exc} increases. Accordingly, a fixed forcing frequency ν produces the maximum amplitude at the undercooling for which $f_{exc} \sim \nu$. For the same reason, the maximum amplitude for the second harmonic 2ν appears at a larger undercooling.

(d) *The effect of anisotropy.* Theoretical considerations and numerical simulations show that anisotropy plays a central role in the formation of dendritic morphology. It is, therefore, reasonable to expect that it has a similar impor-
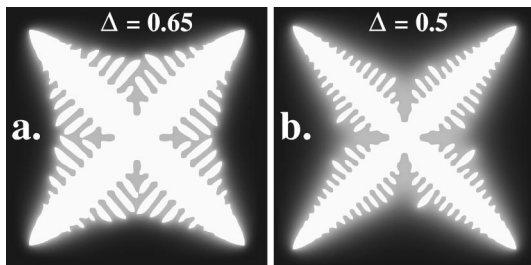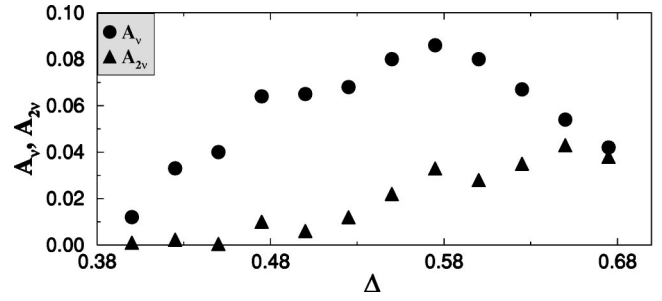

FIG. 9. Amplitude of the Fourier peaks A_ν, $A_{2\nu}$ as a function of undercooling Δ. Other relevant parameters are $\nu=60$, $\xi=0.3$, $a_0=0.16$, $\sigma_4=-0.12$, and $\beta_4=0.24$.

tance in the formation of regular patterns. This expectation is verified by the dependence of growth forms on the magnitude of anisotropies in the system (Fig. 10). The growth patterns and variations of the Fourier amplitudes A_ν and $A_{2\nu}$, and of the symmetry parameters (Fig. 11) indicate that the regularizing effect of external forcing decreases dramatically with vanishing anisotropy, i.e., without well defined orientational preferences the external perturbations are unable to drive the amoebalike growth forms into a regular pattern. This is in accordance with numerical results for directional solidification where the role of the anisotropy in the stability of singlet and doublet cellular patterns was pointed out using a perturbation technique [46]. Note that the tip velocity decreases with decreasing anisotropies (note the difference of simulation times the snapshots correspond to), the excitation with $\nu=60$ generates periodic side arms with increasing spacing.

In these calculations we assumed that both the interfacial free energy and the kinetic coefficient are anisotropic. For the sake of simplicity, their ratio was usually kept constant $\beta_4/\sigma_4=-2$. Our further investigations show, however, that resonance patterns form if *any* of these anisotropies (that of σ or β) is sufficiently large.
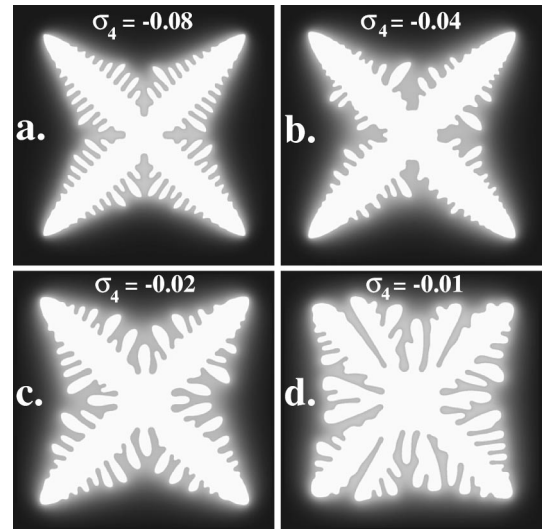

FIG. 10. Pattern formation under periodic forcing as a function of anisotropy: $\sigma_4=-0.08$ (a), $\sigma_4=-0.04$ (b), $\sigma_4=-0.02$ (c), and $\sigma_4=-0.01$ (d). Other relevant parameters are $\Delta=0.55$, $\nu=60$, $\xi=0.3$, $a_0=0.16$, and $\beta_4=-2\sigma_4$. The average growth rate varies with anisotropy, therefore, different times are needed to reach comparable sizes: $t=0.24$ (a), $t=0.3$ (b), $t=0.38$ (c), and $t=0.44$ (d). System size: 1000×1000 pixels.
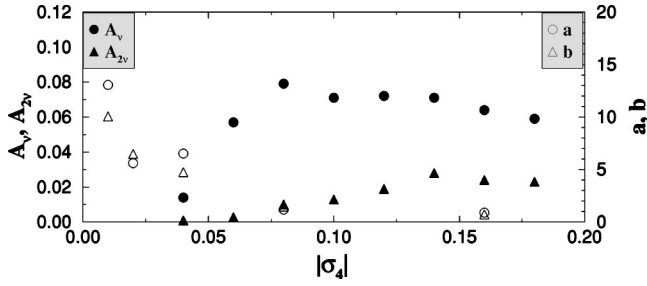

FIG. 8. The effect of undercooling on pattern formation under periodic forcing. (a) $\Delta=0.65$ and (b) $\Delta=0.5$. Other parameters as for Fig. 2(d) except that $t=0.2$ and $t=0.283$ for panels (a) and (b), respectively. System size: 1000×1000 pixels.

FIG. 11. Amplitude of the Fourier peaks A_ν, $A_{2\nu}$, and symmetry parameters a and b as a function of anisotropy parameter $|\sigma_4|$ of the interfacial free energy. The kinetic anisotropy has been varied proportionally $(\beta_4 = -2\sigma_4)$. Other relevant parameters are $\Delta = 0.55$, $\nu = 60$, $\xi = 0.3$, and $a_0 = 0.16$.

3. Modulated heating

(a) *Alternating heating and cooling.* They lead to essentially the same type of resonance patterns as pressure oscillations, provided that the net heat production in a period is negligible. A remarkable difference is, however, that while the average tip velocity v_0 is essentially independent of the amplitude of pressure modulations, it decreases with the amplitude of heat production/extraction (Fig. 12); a phenomenon that might be associated with different efficiencies of heating and cooling.

(b) *Oscillatory heating.* The introduction of a local off-plane thermal transport described by $B(t) = b_0 g(t) + h[u(\mathbf{r},t) - u_\infty]$ was necessary to prevent the melting of the crystal for the heating amplitudes needed to generate regular patterns. Here $h < 0$ is a dimensionless heat transfer coefficient that imitates heat transfer perpendicular to the plane of the liquid crystal layer towards the surrounding of reduced temperature u_∞. Since this term serves as a local heat sink, the in-plane thermal diffusion becomes less restrictive. This results in the formation of more compact objects (see Fig. 13) with thick main arms and less developed side branches. While with an increasing amplitude of the heat pulses the side arms become more regular, they become smaller due to the dissipated heat.

Very similar to pressure modulations, oscillatory heating leads to an oscillating tip velocity. Owing to a decreasing average undercooling accompanied with increasing heating amplitude b_0, the period averaged velocity v_0 of the tip de-
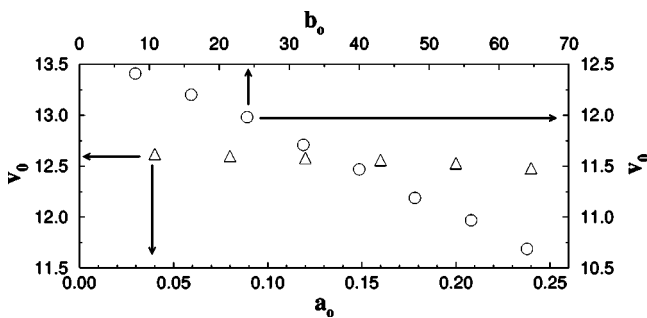

FIG. 12. Average velocity of the tip under periodic heating and cooling (open circles; relevant parameters are $\Delta = 0.6$, $\nu = 60$, $\xi = 0.5$, $\sigma_4 = -0.12$ and $\beta_4 = 0.24$, and for oscillatory pressure [open triangles; calculated with $\langle p \rangle = 0$, $\xi = 0.5$, other parameters as for Fig. 2(d)].
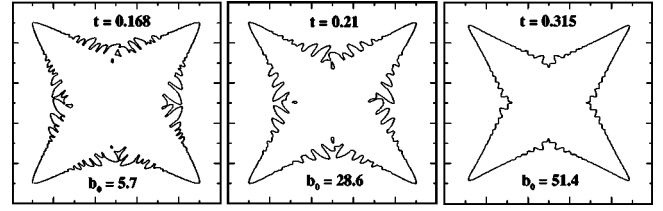

FIG. 13. Pattern contours formed under periodic heat pulses of amplitudes increasing from left to right ($b_0 = 5.7$, $b_0 = 28.6$, and $b_0 = 51.4$). Other relevant parameters are $\Delta = 0.61$, $\nu = 50$, $\xi = 0.15$, $\sigma_4 = -0.16$, $\beta_4 = 0.32$, $h = -14.3$, $\tau_0 = 16$, and $\Delta t = 7 \times 10^{-5}$. System size: 1000×1000 pixels.

creases roughly linearly with b_0 (Fig. 14). At the same time, the amplitude of the oscillatory part of the velocity v_ν increases about linearly. In summary, our investigations imply that under well defined conditions both types of nonlocal forcing can be used to control dendritic growth.

B. Experimental results

In defining the experimental conditions, we utilized the results of computer simulations. For CCH3, the time and spatial resolution of our experimental setup is optimal at an undercooling of ~ 1 K. Comparable variations of the undercooling (~ 0.1–0.2 K) are achievable by applying modulation amplitudes as high as 2 bar or 3×10^{-4} W/cm^2, as estimated on the basis of the pressure coefficient of the equilibrium temperature for the nematic–smectic-B phases (see the Appendix) and other relevant properties.

The appropriate frequency range of forcing has been determined by Fourier analysis of the width $w(t)$ of a freely growing dendrite measured at 66.5 μm behind the tip. Without perturbation, the side branching is essentially random [Figs. 15(a) and 16(a)]. The characteristic frequency, identified as the peak of the broad spectrum in the inset of Fig. 17, is roughly 1.8 Hz. Accordingly, our experimental setup was designed to cover the frequency range of 0–2 Hz.

1. Pressure modulations

The experimental results for pattern formation in the 2 μm thick liquid crystal cell are summarized in Fig. 15. Resonance patterns of fairly regular side-branches are observed [Figs. 15(b)–15(d)] at forcing frequencies comparable with the characteristic frequency of the unperturbed state $\tilde{\nu} \sim 1.8$ Hz. The figure shows germs that nucleated heterogeneously
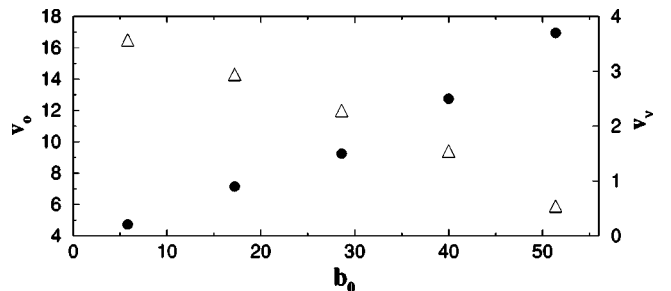

FIG. 14. Average velocity v_0 (open triangles) and amplitude of velocity oscillation v_ν (full circles) as a function of heating amplitude b_0 for simulations presented in Fig. 13.
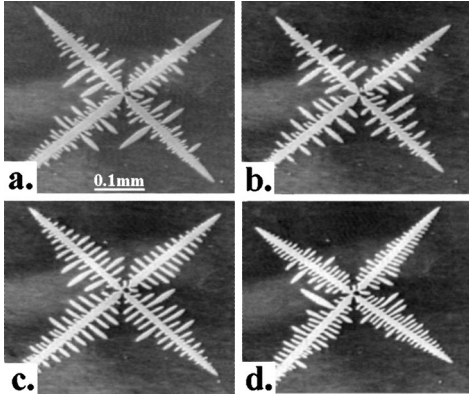
FIG. 15. Snapshots demonstrating the effect of oscillatory pressure on the smectic-B dendrite growing into undercooled nematic phase ($\Delta T = 1.0$ °C). (a) Without pressure oscillations and (b)–(d) with square wave pressure modulation of parameters $p_e = 2$ bar, $\xi = 0.2$, $\tilde{\nu} = 0.75$, 1.18, and 1.96 Hz, respectively.

at the same site with essentially the same orientation several times, yielding reproducible patterns. Although the respective dimensionless undercooling ($\Delta = 0.06$) is considerably smaller than in the simulations ($\Delta = 0.4 - 0.68$), the observed behavior follows closely the predictions of the phase-field theory. This similarity is especially striking when patterns formed at similar reduced frequencies ($\tilde{\nu}/f_0$) are compared [see Figs. 2(c) and 15(b) of $\tilde{\nu}/f_0 = 0.40$ and 0.42 or Figs. 2(d) and 15(c) of $\tilde{\nu}/f_0 = 0.6$ and 0.65]. An interesting observation is that far from the dendrite tip irregularities develop in the lengths of the side branches, despite the even distance of their trunks. We observed an analogous phenomenon driven by the interaction with neighboring side arms via thermal diffusion fields in long-time phase-field simulations [47].

Concerning the effect of the forcing amplitude, we found that pressure oscillations of amplitude of 1 bar regularize the side-branch formation efficiently. With increasing amplitude
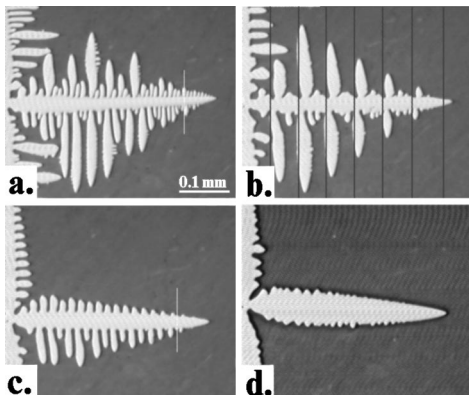

FIG. 16. Snapshots demonstrating the effect of oscillatory heating on the smectic-B dendrite growing into the undercooled nematic phase ($\Delta T = 1.0$ °C). (a) No oscillatory heating; (b) $\tilde{\nu} = 0.2$ Hz, $\bar{P} = 6 \times 10^{-5}$ W/cm^2, $\xi = 0.14$; (c) $\tilde{\nu} = 0.46$ Hz, $\bar{P} = 6 \times 10^{-5}$ W/cm^2, $\xi = 0.16$; (d) $\tilde{\nu} = 0.81$ Hz, $\bar{P} = 1.1 \times 10^{-4}$ W/cm^2, $\xi = 0.61$. The two lines in panels (a) and (c) mark the positions, where the width w of the dendrite has been measured as a function of time (for the Fourier transforms see Fig. 17). Black lines in panel (b) denote the position of the tip at the centers of the heating pulses.
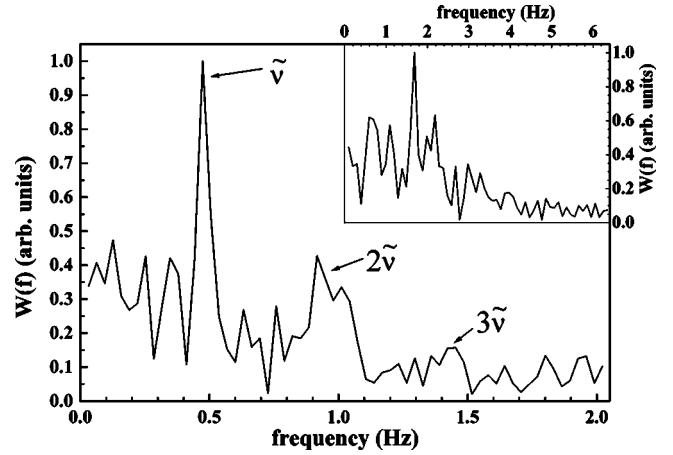

FIG. 17. Fourier spectrum $W(f)$ of the half-width of the dendrite measured 66.5 μm behind the tip as shown in Fig. 16(c). For comparison, the respective spectrum for free dendritic growth [Fig. 16(a)] is also presented (see inset).

the phenomenon becomes more pronounced as predicted by the phase-field calculations. At the largest pressure amplitudes (2 bars) even the secondary side branches correlate with the pressure oscillations.

2. Modulated heating

In analogy to pressure modulations, the periodic heating experiments on the 10 μm thick liquid crystal cell also reveal regular side branching [see Figs. 16(a)–16(c)]. The formation of side branches correlates with the external forcing as illustrated in Fig. 16(b), where the black lines denote the position of the tip at the centers of the heating pulses. The correlation is also evident from the power spectrum of the width of the dendrite measured 66.5 μm behind the tip (Fig. 17). In full accord with the phase-field simulations for asymmetric square waves [Fig. 3(b)], the power spectrum indicates the presence of modes that are either synchronous with the forcing frequency $\tilde{\nu} = 0.46$ Hz, or oscillate with doubled frequency ($2\tilde{\nu}$). Even a peak corresponding to the third harmonic ($3\tilde{\nu}$) may be identified, although with an amplitude that is close to the experimental uncertainty.

Remarkably, in the response to "symmetric" forcing $\xi = 0.5$, the $2\tilde{\nu}$ mode is also present (see the Fourier-spectrum and the short side-arms of doubled frequency in Fig. 18), although this frequency is absent from the forcing spectrum. This finding confirms the nonlinear behavior revealed by phase-field simulations, that higher harmonics missing from the forcing spectrum are also excited [see $W(f)$ for sinusoidal forcing in Fig. 3].

Increasing the heating amplitude or ξ so that the period-averaged heating power reaches $\bar{P} \approx 10^{-4}$ W/cm^2, the formation of the side branches is suppressed [see Fig. 16(d)], a phenomenon resembling that seen in the numerical simulations (Fig. 13). Further increase of the heating amplitude (and power) melts the dendrites back.

In line with our theoretical predictions (see Fig. 2 of Ref. [33]), a weak oscillation of the tip velocity has been observed that correlates with the forcing. However, its amplitude is just above the resolution of the present experimental setup.
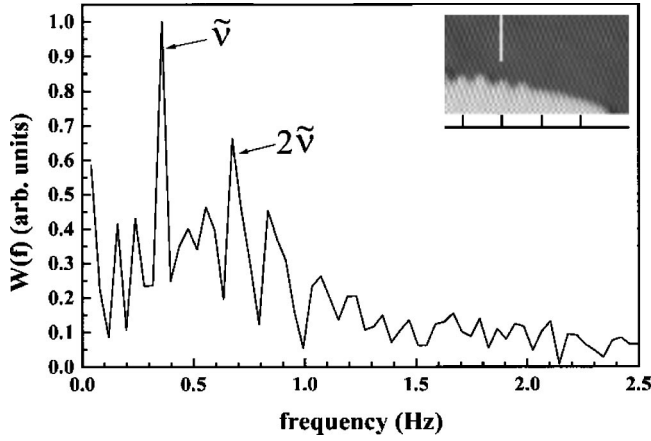
FIG. 18. Side branch formation close to the tip under ''symmetric'' ($\xi=0.5$) square-wave heating as displayed by a smectic-B dendrite growing into the undercooled nematic phase. The growth pattern (insert) and the Fourier spectrum $W(f)$ (main frame) are shown. Black lines in the inset denote the forcing frequency $\tilde{\nu}$. The white line marks the position (53.2 μm behind the tip) where the width w of the dendrite has been measured as a function of time. Note the presence of the mode oscillating with twice the base frequency of forcing; a mode missing from the forcing spectrum. The relevant parameters are $\tilde{\nu}=0.35$ Hz and $\bar{P}=9\times10^{-5}$ W/cm^2.

A remarkable feature of the ''regularized'' dendrites, not seen in the simulations, is a shift in the position of the side branches on the two sides of the main tip [see, e.g., Figs. 16(b) and 16(c)]. As a result, one cannot use the symmetry parameters a and b [defined by Eqs. (3) and (4)] for characterization of the pattern's regularity. For the same reason, the Fourier spectra shown in Figs. 17 and 18 have been evaluated from the half-width of the dendrite. Despite the shift of the side branches, the power spectra on the two sides are fairly similar.

The shift in the position of the side branches might be attributed to the asymmetry of the dendrite tip (due to the angular dependence $\sigma(\theta)$ [35]), observed at higher resolution of the tip region—one side of the tip was faceted. The first observable surface undulation that evolves later into a side-arm appears on the rounded side. In contrast, the faceted side remains smooth up to the same distance behind the tip.

Finally, one should mention that the electric heating in liquid crystals may have side effects that are not incorporated into our phase-field model. Switching the electric field on, the orientation of the nematic director $\mathbf{n}(N)$ changes from planar to homeotropic (perpendicular to the bounding plates), an effect that influences the magnitude and anisotropy of the interfacial free energy, and may induce local flow in the sample. However, these side effects are of minor importance, since they are present in full strength much below the electric field needed for regularization.

V. DISCUSSION

In this section we compare our results with those on the dynamic response of dendritic growth to local forcing with fixed frequency as emerging from the microscopic solvability theory (MST) and experiment. It is appropriate to mention that some features of the MST derivation prevent a quantitative comparison. For example, the MST calculations were performed for a 2D symmetric dendrite, while the anisotropy, the stability coefficient, and the Péclet number were assumed to be small; conditions that are not met in our simulations and experiments. Therefore, a qualitative comparison is only meaningful. An important further difference between previous work and ours is that we used nonlocal forcing, as opposed with the tip-localized forcing assumed in the MST.

Let us first recall some of the MST predictions on noise amplification (based on the Wentzel-Kramers-Brillouin approximation) that have been tested by comparison with numerical simulations [45,48] and experiments [30] for fixed frequency perturbations localized at the tip.

(i) Periodic forcing by a fixed frequency ν leads to surface oscillations of amplitude that increases exponentially with the distance from the dendrite tip up to a critical distance ζ_c proportional with $1/\nu^4$. For larger distances the amplitude decreases and eventually dies away. If, in turn, the distance from the tip is fixed and ν is varied, a peak is observed in the amplitude.

(ii) The localized wave packets behave differently; they grow exponentially as they move to arbitrarily large distances from the tip, while the respective characteristic wave length increases. Our simulations are in line with the previous MST and numerical predictions for tip-localized forcing in the following respects.

(a) In the vicinity of the dendrite tip, the amplitude of the mode synchronous with forcing increases roughly exponentially with the distance ζ from the tip. Owing to the excessive computation time and memory needed, we were unable to study the decay of this mode in detail. Nevertheless, as expected from the MST, at large frequencies [Fig. 2(f)] the synchronous mode can only be recognized in the vicinity of the dendrite tip. Another sign, that accords with the presence of a critical distance ζ_c beyond which the excited mode decays, is a maximum observed in the amplitude $A_{2\nu}$ of the second harmonic (Fig. 6) in simulations where the forcing spectrum contains 2ν with a significant amplitude.

(b) The amplitude A_ν measured at a fixed distance behind the dendrite tip shows a maximum as a function of the forcing frequency [Fig. 5(a)].

An interesting feature, revealed by our phase-field simulations, is that besides the synchronous mode, the Fourier spectrum of the dendrite width contains the second and third harmonics with perceptible amplitudes. This finding is confirmed by our experiments. We believe that this is the first direct demonstration of such nonlinear effects in connection with diffusional instability induced dendrite formation during a first-order phase transformation. It appears, that this non-linear behavior is not a peculiarity of spatially homogeneous forcing. Although not mentioned in the original works, traces of higher harmonics seem to be present in the respective power spectra for local forcing as well [32,30]. It is worth mentioning, furthermore, that a similar behavior has been observed in the case of anomalous Saffman-Taylor fingering [35], suggesting that the appearance of higher harmonic modes in response to periodic external forcing is a common feature of dendrite formation whether driven by diffusional or mechanical instabilities. It is remarkable that the appearance of higher harmonics has been reported during the time evolution of spatially perturbed planar interface in

directional solidification [46]. Further work is needed, however, to clarify whether the two phenomena have a common origin. Summarizing, in the present state of affairs it seems that the only specific feature of pattern formation under nonlocal forcing is a simultaneous triggering of side branches (of first, second, and higher orders) on independent crystallites throughout the sample.

VI. SUMMARY

Our computer simulations and experiments demonstrated that the dendritic morphology can be regularized by nonlocal time-periodic forcing realized by modulated pressure and Joule heating. These conditions lead to an oscillatory velocity of the dendrite tip, and yield side branches at regular distances, provided that the frequency of the modulation is close to the ''natural'' frequency of free side-branch formation. The dynamic response of the system to such nonlocal forcing can be understood in general on the basis of previous theoretical and experimental results on tip-localized forcing. However, the nonlinear effects, such as the appearance of higher harmonic modes, warrant further theoretical work.

ACKNOWLEDGMENTS

APPENDIX: PRESSURE DEPENDENCE OF THE PHASE TRANSITION TEMPERATURE

The pressure dependence of the N–S_B phase transition temperature has been measured by a procedure similar to that described in Ref. [37]. For different p_e a single S_B monodomain has been kept at constant size by controlling the temperature for several hours (until the thermodynamic equilibrium state of the system has approached). Figure 19 shows
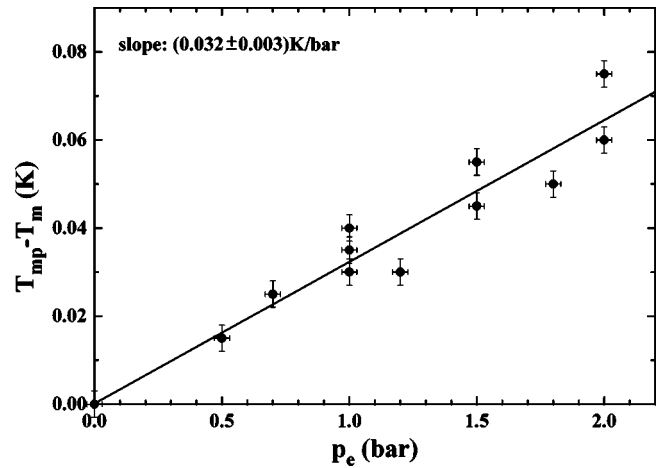

FIG. 19. Pressure dependence of the temperature of the nematic-smectic-B phase transition.

the change of the phase transition temperature depending on the pressure. Linear fit on the data gives a slope $dT_m/dp = (0.032 \pm 0.003)$ K/bar for the Clapeyron coefficient.

The Clapeyron coefficient can be also calculated from the relation

$$\frac{dT_m}{dp} = \frac{T_m^0 \Delta V_{N \to SB}}{\Delta H}, \tag{A1}$$

where T_m^0, $\Delta V_{N \to SB}$ and ΔH are the phase transition temperature at atmospheric pressure, the molar volume change on transition, and the molar latent heat of fusion, respectively. From the relevant material parameters of CCH3, namely, $T_m^0 = 329.45$ K [37], $m = 233$ (molar mass), $\rho = 895.4$ kg/m³ (density at 80.6°C [49]), $\Delta H = 6247$ J/mol, $\Delta V_{N \to SB}/V = -2.6\%$, and $\alpha_N = 25 \times 10^{-4}$ 1/K (volumetric expansion coefficient in the nematic phase [50]) one obtains $dT_m/dp = 0.033$ K/bar in excellent agreement with the experimental value.

Although this value is much larger than for metals, it is not unusual for liquid crystals. For example, ~0.03 K/bar has been reported for the nematic-crystal transition in PAA, and ~0.1 K/bar for the nematic smectic transition in p-methoxybenzoic acid [51]. Comparable, or even larger coefficients have been measured on other organic substances such as camphene 0.214 K/atm, pivalic acid 0.0674 K/atm, and succinonitrile 0.0245 K/atm [52].

[1] M. C. Cross and P. C. Hohenberg, Rev. Mod. Phys. **65**, 851 (1993).

[2] E. Ben-Jacob, O. Shochet, A. Tenenbaum, I. Cohen, A. Czirók, and T. Vicsek, Fractals **2**, 15 (1994).

[3] J. P. Gollub and J. S. Langer, Rev. Mod. Phys. **71**, S396 (1999).

[4] *Handbook of Crystal Growth*, edited by D.T.J. Hurle (North-Holland, Amsterdam, 1993), Vol. 1B.

[5] E. Ben-Jacob, O. Shochet, A. Tenenbaum, I. Cohen, A. Czirók, and T. Vicsek, Phys. Rev. E **53**, 1835 (1996).

[6] E. Ben-Jacob and P. Garik, Physica D **38**, 16 (1989).

[7] J. Németh, G. Papp, C. Ngó, and M. Barranco, Phys. Scr. T. **32**, 160 (1990).

[8] F. C. Adams, K. Freese, and J. S. Langer, Phys. Rev. D **47**, 4303 (1993).

[9] J. S. Langer, R. F. Sekerka, and T. Fujioka, J. Cryst. Growth **44**, 414 (1978); Y. Furukawa and W. Shimada, *ibid.* **128**, 234 (1993).

[10] S. C. Huang and M. E. Glicksman, Acta Metall. **29**, 701 (1981).

[11] M. E. Glicksman and N. B. Singh, J. Cryst. Growth **98**, 277 (1989).

[12] E. R. Rubinstein and M. E. Glicksman, J. Cryst. Growth **112**, 84 (1991); **112**, 97 (1991).

[13] U. Bisang and J. H. Bilgram, Phys. Rev. Lett. **75**, 3898 (1995).

[14] J. Bechhoeffer, in *Pattern Formation in Liquid Crystals*, edited by Á. Buka and L. Kramer (Springer, New York, 1996), p. 257.

[15] R. Pieters and J. S. Langer, Phys. Rev. Lett. **56**, 1948 (1986).

[16] A. Dougherty, P. D. Kaplan, and J. P. Gollub, Phys. Rev. Lett. **58**, 1652 (1987).

[17] M. Georgelin and A. Pocheau, Phys. Rev. E **57**, 3189 (1998).

[18] A. Karma and W. J. Rappel, Phys. Rev. E **60**, 3614 (1999).

[19] *Handbook of Crystal Growth* (Ref. [4]), p. 1077.

[20] M. Ben Amar and Y. Pomeau, Europhys. Lett. **2**, 307 (1986).

[21] D. C. Hong and J. S. Langer, Phys. Rev. A **36**, 2325 (1987).

[22] J. S. Langer, Phys. Rev. A **36**, 3350 (1987).

[23] O. Penrose and P. C. Fife, Physica D **43**, 44 (1990).

[24] R. Kobayashi, Physica D **63**, 410 (1993).

[25] S.-L. Wang, R. F. Sekerka, A. A. Wheeler, B. T. Murray, S. R. Coriell, R. J. Braun, and G. B. McFadden, Physica D **69**, 189 (1993).

[26] R. Kobayashi, Exp. Math. **3**, 59 (1994).

[27] A. Karma and W. J. Rappel, Phys. Rev. Lett. **77**, 4050 (1996).

[28] A. Karma and W. J. Rappel, Phys. Rev. E **57**, 4323 (1998).

[29] X. Qian and H. Z. Cummins, Phys. Rev. Lett. **64**, 3038 (1990).

[30] L. Williams, M. Muschol, X. Qian, W. Losert, and H. Z. Cummins, Phys. Rev. E **48**, 489 (1993).

[31] B. T. Murray, A. A. Wheeler, and M. E. Glicksman, J. Cryst. Growth **154**, 386 (1995).

[32] Ph. Bouissou, A. Chiffaudel, B. Perrin, and P. Tabeling, Europhys. Lett. **13**, 89 (1990).

[33] T. Börzsönyi, T. Tóth-Katona, Á. Buka, and L. Gránásy, Phys. Rev. Lett. **83**, 2853 (1999).

[34] Pressure modulation has been used previously to influence viscous fingering [35], where it has a mechanical effect on the interface, while in our case pressure modulation exerts thermodynamic effect on crystal growth. Another difference is that in the case of viscous fingering pressure modulation acts on a single germ, while the growth of crystals is influenced throughout the sample in a spatially homogenous manner.

[35] M. Rabaud, Y. Couder, and N. Gererd, Phys. Rev. A **37**, 935 (1988).

[36] Á. Buka, T. Tóth-Katona, and L. Kramer, Phys. Rev. E **51**, 571 (1995).

[37] T. Tóth-Katona, T. Börzsönyi, Z. Váradi, J. Szabon, Á. Buka, R. González-Cinca, L. Ramirez-Piscina, J. Casademunt, and A. Hernández-Machado, Phys. Rev. E **54**, 1574 (1996).

[38] T. Börzsönyi, Á. Buka, and L. Kramer, Phys. Rev. E **58**, 6236 (1998).

[39] Hypercooling limit/unit undercooling: that temperature/ undercooling at which the enthalpy of freezing heats the solid up to its melting point $T_m - T_{\text{hyper}} = L/c_p$.

[40] H. Löwen, J. Bechhoefer, and L. S. Tuckerman, Phys. Rev. A **45**, 2399 (1992).

[41] W. W. Mullins and R. F. Sekerka, J. Appl. Phys. **34**, 323 (1963); **35**, 444 (1964); R. J. Braun, G. B. McFadden, and S. R. Coriell, Phys. Rev. E **49**, 4336 (1994).

[42] G. B. McFadden, A. A. Wheeler, R. J. Braun, and S. R. Coriell, Phys. Rev. E **48**, 2016 (1993).

[43] The quantity $1 - \phi$, where $\phi(\mathbf{r}, t)$ is the phase field, is akin to the structural order parameter emerging from the local Gaussian approximation used in the density functional theory of freezing [Y. C. Shen and D. W. Oxtoby, J. Chem. Phys. **104**, 4233 (1996)].

[44] Y.-T. Kim, N. Provatas, N. Goldenfeld, and J. Dantzig, Phys. Rev. E **59**, R2546 (1999).

[45] M. N. Barber, A. Barbieri, and J. S. Langer, Phys. Rev. A **36**, 3340 (1987).

[46] W. Losert, D. A. Stillmann, H. Z. Cummins, P. Kopczyński, W.-J. Rappel, and A. Karma, Phys. Rev. E **58**, 7492 (1998).

[47] Computer animations based on our simulations are shown at URL www.kfki.hu/~btamas/phase/perturb.html

[48] D. Kessler and H. Levine, Europhys. Lett. **4**, 215 (1987).

[49] S. Asahina, M. Sorai, and R. Eidenschink, Liq. Cryst. **10**, 675 (1991).

[50] D. Grasso, S. Fasone, G. di Pasquale, and F. Castelli, Thermochim. Acta **140**, 31 (1989).

[51] R. Shashidhar and S. Chandrasekhar, J. Phys. (Paris) **36**, C1-49 (1975).

[52] J. C. La Combe, M. B. Koss, L. A. Tennenhouse, E. A. Winsa, and M. E. Glicksman, J. Cryst. Growth **194**, 143 (1998).